




Influence of porous silicon as thermal insulation layer on the structural, optical, electrical and temperature responsive properties of Mn–Co–Ni–O NTC thin films

Bo Yang^{1,2}, Yuxian Song^{1,2}, Xinmiao Wang^{1,2}, Zhaoyang Chen¹, Pengjun Zhao¹,
Aimin Chang¹, Bo Gao¹, and Wenwen W. Kong^{1,*} 

¹Key Laboratory of Functional Materials and Devices for Special Environments of CAS, Xinjiang Key Laboratory of Electronic Information Materials and Devices, Xinjiang Technical Institute of Physics & Chemistry of CAS, Urumqi 830011, China

²Center of Materials Science and Optoelectronics Engineering, University of Chinese Academy of Sciences, Beijing 100049, China

Received: 26 March 2023

Accepted: 11 June 2023

Published online:
20 June 2023

© The Author(s), under
exclusive licence to Springer
Science+Business Media, LLC,
part of Springer Nature 2023

ABSTRACT

The temperature response rapid of Mn–Co–Ni–O (MCNO) thin film within excellent NTC charters is limited by the heat transfer between the film and its substrate. To settle the bottleneck, the porous silicon (PS) as thermal insulation layer was brought forward. Although both MCNO/SiO₂/Si and MCNO/SiO₂/PS/Si films exhibited typical polycrystalline spinel structure, the (220) and (400) XRD peak strength as well as Raman active mode (around ca. 290 cm⁻¹) changed represent the tensile stress appearing on the surface of the PS layer. From spectroscopic ellipsometer spectroscopy, it was found that the maximal refractive index of the MCNO thin film was more than twice as to the value of films with PS layer. However, it had little influence on the electrical properties as thermal constants (3515 and 3469 K) were similar even the high-frequency vibration experiments employed. The FEA simulation result showed that the PS layer forms a high interface thermal resistance due to the low thermal conductivity of the air in the pores of PS. The MCNO/SiO₂/PS/Si composite film captured faster response time (11 ms) compared to the MCNO films on SiO₂/Si substrates (345 ms). It will open a way to design an ultra-fast response NTC film thermistor by substrate modification.

1 Introduction

For environment with highly dynamic temperature variations, such as ocean turbulence where water mass boundaries are superimposed with each other and different layers have a temperature gradient, the

measurement error of temperature sensor due to its own thermal time constant will be particularly important [1, 2]. It is imperative to develop a temperature sensor with ultra-fast response characteristic to reduce this response hysteresis. To produce faster responding commercial thermistors, the sensitive,

Address correspondence to E-mail: kongww@ms.xjb.ac.cn

packaging and mounting materials that indirectly affect the thermal time constant of thermistors have all attracted the attention of researchers [3, 4]. After the systematic investigation and study, it is found that the thermal time constant of thermistor mainly depends on the heat capacity, which is proportional to the device dimensions. As the physical limit of the size of the thermal ceramic is close to the micron level, it is significant to explore the film thermistors, which can be controlled in the tens to hundreds of nanometers [5, 6].

The Mn–Co–Ni–O (MCNO) system material with spinel structure is one of the most commonly used NTC film materials because of its excellent negative temperature coefficient, good stability and fast response [7–9]. The Si/SiO₂ substrate with economic and integration advantages may make it preferable to develop fast response thermistor devices using film grown thereon [10–12]. Therefore, various researches have been carried out around the MCNO/SiO₂/Si structure to improve the response rapid. However, the high thermal conductivity of the Si based substrate (156 W/cm °C) will cause thermal conduction between the film and the substrate [13, 14]. This will invisibly increase the capacity of the sensitive unit, thereby causing an increase in the response time of the ceramic film material. Therefore, it is crucial to build a stable and efficient thermal insulation structure on Si/SiO₂ substrate to fabricate fast thermal response sensor. There are two main methods to achieve thermal insulation in temperature sensors. One of the methods is to process the suspended structure by micro-mechanical technology, but it cannot function stably and effectively due to the weaker mechanical strength and the longer manufacturing process [15–17]. Another method is to directly deposit materials with relatively low thermal conductivity such as quartz, organic polymers, fiber materials and various aerogel, but they are not compatible with standard IC technology and cannot be adapted to large-scale mass production [18–22]. In the present decades, porous silicon has attracted considerable interests due to its large effective surface area for potential application in the development of silicon-based thermal devices. Compared with these materials, the porous silicon (PS) with special structure has excellent mechanical properties, mature preparation process and compatibility with the IC technology, which provides an effective solution to the above problems [23, 24].

In this paper, MCNO films were grown on SiO₂/Si and SiO₂/PS/Si substrates by magnetron sputtering. In which the overall heat capacity increases significantly due to the bulky substrate, which is detrimental to the fast response of the sensor. Therefore, to reduce this detrimental effect, porous silicon is introduced as an adiabatic buffer layer to reduce the heat transfer between the film and the substrate, ultimately achieving a lower heat capacity and a higher response rate. The surface morphology, crystal structure and optical properties of the film were characterized, which were expected to obtain the impact of introducing the PS buffer layer on the performance of the thin film. In the future, we will conduct further research from the perspective of structural design, hoping to obtain a temperature sensor with faster response speed.

2 Experimental

2.1 Sample preparation

The Mn–Co–Ni–O (MCNO) thin films were prepared by magnetron sputtering method using a ceramic target. The MCNO ceramic films are deposited on SiO₂/Si, SiO₂/PS/Si substrates, where PS is the abbreviation for porous silicon. Among them, SiO₂ serves as the electrical insulation layer, porous silicon buffer layer serves as the thermal insulation layer, and Si only plays a supporting role. The substrate with PS layer was fabricated by Sil'tronix Silicon Technologies Co. Ltd. Before ceramic films deposition, all the substrate with an area of 10 × 10 mm² were cleaned with acetone, alcohol and deionized water in sequence. Afterwards, substrates were placed on the sample platform in the chamber. Prior to films preparation, the base pressure was evacuated to be 8.0 × 10⁻⁴ Pa and the high purity (99.99%) argon gas pressure was 1.0 Pa to provide the plasma. After depositing 20 min at 150 °C and 40 W in the sputter chamber, all the as-prepared films were annealed at 750 °C for 30 min [25–28].

2.2 Characterizations and measurements

The surface morphologies of the MCNO ceramic films were represented by atomic force microscopy (AFM, Asylum Research MFP-3D-SA) in tapping mode and field emission scanning electron

microscope (FE-SEM, LEO 1430VP, Germany). The crystal structures of the MCNO thin films were characterized through X-ray diffraction (XRD, Bruker D8 Advance, Germany) with Cu K α radiation in the range from 20 to 80°. The composition and cations analysis in these films were characterized by X-ray photoelectron spectroscopy (XPS, Shimadzu AXIS-ULTRA DLD) with Al K α radiation ($h\nu = 1486.6$ eV). type background blended with a linear background subtraction was used to compute the peak intensities by adopting the XPS peak software. The optical spectra were obtained by a spectroscopic ellipsometer (SE, Sentech SE850) and the obtained data of the samples were fitted by the double Tauc-Lorentz (DTL) dispersion function. The lattice vibrations of films were analyzed by Raman spectroscopy (Thermo Scientific DXR; America). The resistance–temperature (R–T) relationship of the MCNO thin films was measured between -5 to 50 °C using a computer-controlled source meter (Agilent Keithley 2410, America). The response times were monitored in the ice-water conditioned environment using a system based on the Oscilloscope (Tektronix OPO7354, America).

3 Results and discussions

3.1 Surface morphology and crystal structure

Figure 1 shows the surface morphology of MCNO film samples sputtered on SiO₂/Si and SiO₂/PS/Si substrates, corresponding to S1 and S2, measured by FESEM and the AFM. It illustrates that both the two samples are uniform and no cracks. Although the thicknesses of the two films are both nearly 165 nm as shown in the insets of Fig. 1a and b, the density become slightly worse while the PS layer was employed in the substrate. It directly depends on the rough surface of insert PS layer which is also shown in the insets. It may also lead to the increase of grain boundary resistance. The AFM images have been analyzed here and found that the root mean square roughness (R_q) are 0.2 and 3.2 nm for MCNO/SiO₂/Si and MCNO/SiO₂/PS/Si, which demonstrates that the adding of PS layer has significant effect on the surface morphology of the MCNO films.

Both the two films exhibited a typical polycrystalline spinel structure according to the PDF card No.

23-1237 [29], as can be seen from the grazing incidence X-ray diffraction pattern (Fig. 2a). The peak positions including (220), (311), (400), (511), and (440) can be observed, with the strongest peak detected at (311). As the addition of PS layer, all peak positions do not shift, but the (220) peak of S1 is stronger than S2, whereas the (400) peak of S2 is stronger than S1. This phenomenon might depend on the difference of film roughness. To further confirm whether the PS layer affect the crystal structure, Raman analysis was carried out.

Figure 2b shows the Raman spectra for S1 and S2 at room temperature in the range 400–1000 cm⁻¹ [30]. There are two major vibration modes located at ~ 290 and ~ 520 cm⁻¹. The Raman peaks located at around 290 cm⁻¹ are assigned to the T_{2g} mode, which is associated with Mn–O bond stretching vibrations of the tetrahedral site ions [31]. The sharp peak at 520 cm⁻¹ is due to the silicon substrate [32]. Compared with the standard spectral peak (290 cm⁻¹) of S1, the spectrum of S2 shifts to a lower frequency and broadens asymmetrically on the low energy side. The negative Raman shift indicates tensile stress appearing on the surface of the porous silicon layer.

3.2 Optical properties

Figure 3a show the relationship between refractive index n and wavelength (λ) of samples measured by spectroscopic ellipsometry, which often has been used for studying the optical properties of MCNO thin films [33–35]. In this case, two models (Air/MCNO/SiO₂/Si and Air/MCNO/SiO₂/PS/Si) are used to describe the ellipsometry parameters of the samples. The mean-square-root error of the fitting curve between model inversion and real structure is 0.48, which indicates the curve fitted by the spectra ray software has good fitting quality. The input fitted thickness of the films for S1 and S2 are 162 and 166 nm, which come from the cross-section SEM images. After analysis the ellipsometry results, the refractive index (n), extinction coefficient (k) values as a function of wavelength (λ) for S1 and S2 can be obtained as shown in Fig. (3), which illustrates that the adding of PS in the films has a significant influence on the plot shape. The maximal n value of the S1 film is 3.78, which is more than twice as likely to the value of 1.59 for S2 film. This means that the refractive index decreases while the PS layer were added. Figure 3a shows the n – λ plots of the films. S2 shows

Fig. 1 a, c SEM and AFM images of the S1 and b, d SEM and AFM images of the S2

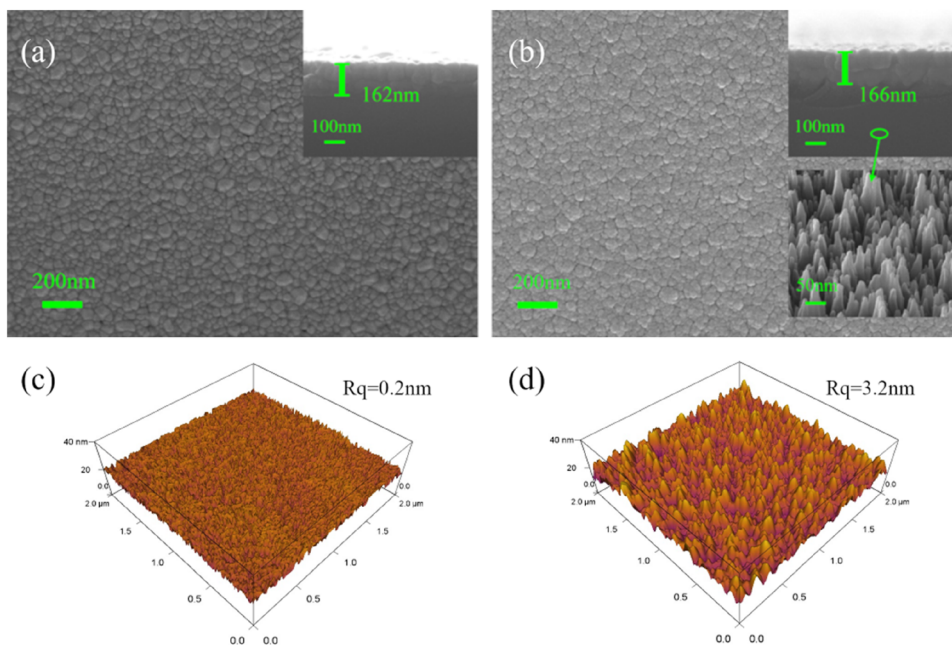


Fig. 2 a XRD patterns and b Raman spectra of S1 and S2

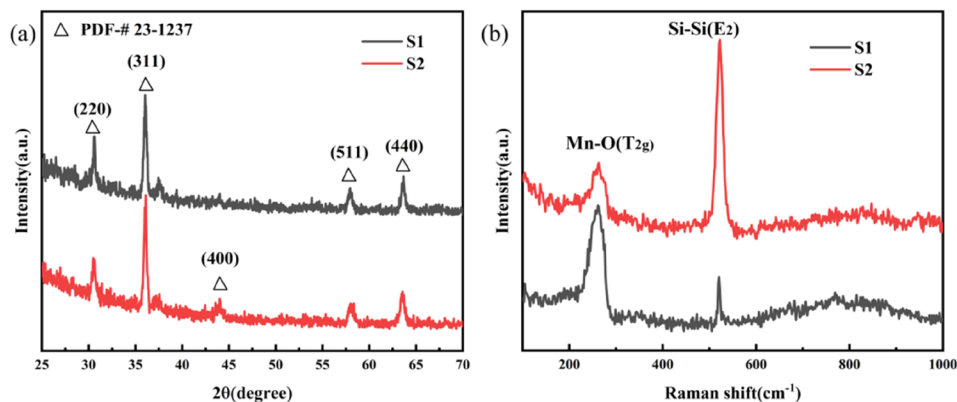
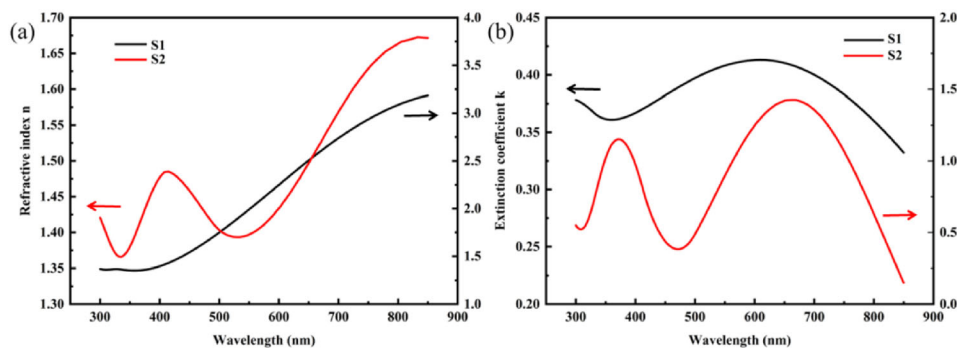


Fig. 3 a Refractive index n , b extinction coefficient k as a function of wavelength for S1 and S2



one excitation peak in the wavelength range of 350–500 nm. However, there is no peak and the refractive index steps up as the wavelength increases in the S1 film. Figure 3b shows the k - λ plots of the films. Contrary to refractive index, the extinction

coefficient of S1 is significantly lower than that of S2. Two peaks of S2, at 375 and 665 nm, are observed, which are attributed to the critical points of the MCN materials. However, S1 film only contains a very wide peak and the k value fluctuates in a small range

of 0.33–0.42. The Spectroscopic Ellipsometry is very sensitive to the surface morphology of the thin film, which ultimately leads to these different results.

3.3 Cation distribution

XPS is used to detect the oxidation state of elements on the surface of films, which provides relevant evidence of the combined state of Mn, Co, Ni and O elements [25, 36]. Figure 4 shows the XPS fitting results of Mn 2p_{3/2}, Co 2p_{3/2} and Ni 2p_{3/2} in the films. Both the Mn 2p_{3/2} peak for S1 can be deconvoluted into three sub-peaks at 641.3, 642.5 and 644.5 eV, attributing to Mn²⁺, Mn³⁺, and Mn⁴⁺. The ratios of Mn²⁺:Mn³⁺:Mn⁴⁺ were found to be 0.98:1.45:1 and 1.02:1.43:1 for S1 and S2. The peak intensity was also estimated by the peak synthesis procedure, inclusive of Co²⁺ (782.1 eV), Co³⁺ (780.1 eV) and Ni²⁺ (854.6 eV). According to the area of its corresponding peak, the ratios of Co²⁺/Co³⁺ were found to be 0.47 and 0.44 for S1 and S2, respectively. The Ni 2p_{3/2} shows one obvious peak labeled as Ni²⁺ (854.7 eV) and another satellite peak (861 eV). It demonstrates that the Ni element exists in the form of Ni²⁺ in all films. The measured areas of peaks are corrected by atomic sensitivity factors of 2.659 for the Mn 2p_{3/2}, 3.590 for Co 2p_{3/2} and 4.044 for Ni 2p_{3/2} in order to obtain elemental oxygen-to-metal ratios (less than 10% error). All the proportion of cations with different valence states were calculated and are summarized in Table 1.

A comparison of the two samples indicates no apparent variation in the binding energies of each element. It can be seen from Table 1 that the proportion of valence states of each element changes slightly, with Mn⁴⁺ and Mn³⁺ decreasing by about 1% and 1.3% respectively, and Co³⁺ increasing by 2.7%. In manganese-based spinel, the electrical conductivity depends on the Mn³⁺ and Mn⁴⁺ concentration or hopping distance [37]. Therefore, the difference in the ratio of Mn³⁺/Mn⁴⁺ will ultimately be reflected in the change of resistivity.

3.4 Electrical properties

Figure 5a shows the relationship between resistance (R) and temperature (T) of films in the temperature range of –5–50 °C. The resistance of both samples decreases with the ambient temperature increasing, which illustrates that the resistance of both samples

decreases exponentially with increasing temperature, which can be described by Arrhenius Relationship [38]:

$$R = R_0 \exp[E_a/(k_B T)], \quad (1)$$

where E_a is the activation energy, k_B is the Boltzmann constant, B is the thermal constant, which is usually used to characterize the temperature sensitivity of the thermistors. The resistance of S2 is slightly larger than that of S1. The electrical conduction of MCNO is considered to be accomplished by small polaron hopping conduction [39]. The hopping of small polaron between Mn³⁺ and Mn⁴⁺ is the major factor of the electron transport of Mn-based spinel oxides. As discussed previously, the ratio of Mn³⁺/Mn⁴⁺ for S2 is lower than that for S1, that indicates the electron density decreases, and the carrier concentration also decreases, which is ultimately manifested by increases in its resistance. In addition, the decrease of film density also contributes to the increase of resistance. The $\ln R - 1/T$ plots for the MCNO thermistors is fitted and shown in Fig. 5(b). It is found that the slope of the two sample is extremely close to each other, which demonstrates the similar thermal constant. Usually, the thermal constant $B_{25/50}$ value can be calculated by the following Eq. (2) [40]:

$$B_{25/50} = \ln(R_{25}/R_{50})/(1/T_{25} - 1/T_{50}), \quad (2)$$

where R_{25} and R_{50} represent the resistance at the temperature 25 °C and 50 °C, respectively. The calculated results of the $B_{25/50}$ of the two film samples are 3515 K and 3469 K, which can be explained by the electronic transport in Mn-based spinel oxides, that is, the hopping of small polarons between Mn³⁺ and Mn⁴⁺ [25]. The B value increases as the decreased of the Mn³⁺/Mn⁴⁺ ratio. Although the MCNO thin films on the Si substrates display similar electrical performance due to the similar crystal structure and cation distribution, the effect of PS layer on mechanical strength of films should be validated indirectly by testing the resistance after for high-frequency vibration.

High-frequency vibration is often regarded as the simple method to predict the electronic components' lifetime [41]. Considering the stability of the porous structure of silicon, two samples were selected for high-frequency vibration experiments. The frequency varied in the range of 10.0–2.0 kHz, the logarithmic frequency was swept 12 times, 20 min each time. Figure 5c and d show both of the samples have the

Fig. 4 a and b Mn $2p_{3/2}$, c and d Co $2p_{3/2}$, e and f Ni $2p_{3/2}$ XPS spectra of S1, S2, respectively

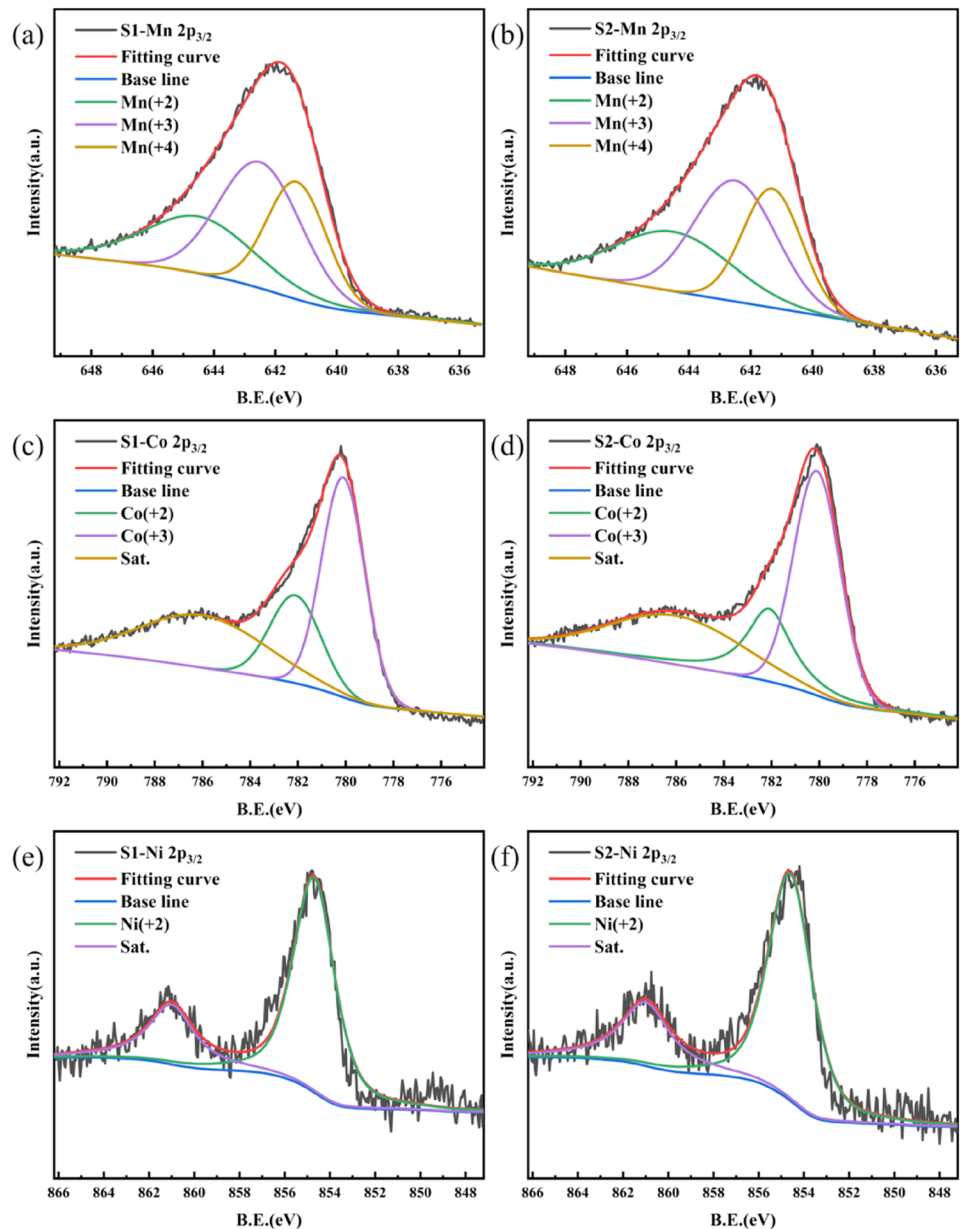


Table 1 All cations distribution in MCNO films of S1 and S2

Sample	Mn ⁴⁺ (%)	Mn ³⁺ (%)	Mn ²⁺ (%)	Co ³⁺ (%)	Co ²⁺ (%)	Ni ²⁺ (%)
S1	16.71	24.28	16.45	23.37	11.01	8.18
S2	15.72	22.61	16.01	26.05	11.55	8.07

similar R–T relationship and excellent linearity, which proves that the film’s electrical properties are not affected by the high-frequency vibration. This indicates that the films with the addition of the porous silicon layer is relatively stable.

3.5 Temperature responsive properties

The air thermal resistance material has been provided by the interval of PS layer in the MCNO thin films, which benefits for the interference elimination of substrate during thermal transfer in the films and then improves the response speed. By comparing the

Fig. 5 **a** The R–T curves **b** $\ln R—1000/T$ for S1 and S2, **c** the R–T curves **d** $\ln R—1000/T$ curves for S1 and S2 before and after vibration

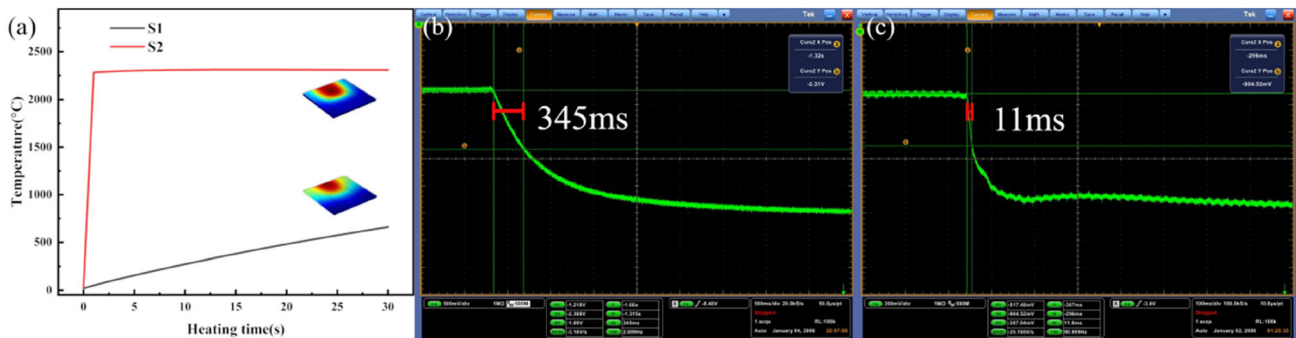
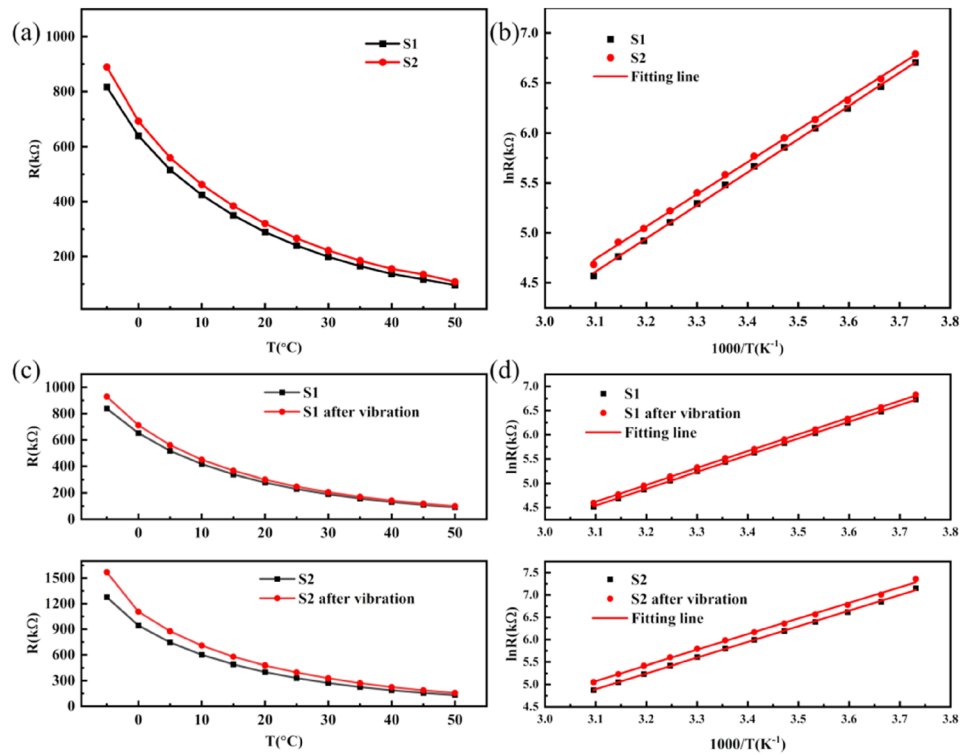


Fig. 6 **a** The heating model and temperature distribution; **b, c** the response time of S1 and S2

simulation results of two NTC thin film thermistor three-dimensional models of traditional silicon substrate and porous silicon substrate in Fig. 6a, the influence of thermal insulation structure porous silicon on the performance of the thermal unit is analyzed. In this model, PS layer added between SiO₂ and Si is used to limit thermal conduction between the substrate and the film to reduce the flow of heat. There is a large gap between the time and the final temperature for the temperature rise of the two models when they were heated for 30s. Therefore, as can be seen that growing a PS buffer layer between the NTC thermal film and the Si substrate can effectively isolate the heat transfer between the thermal

film and the substrate, which is of great help in reducing the response time [42, 43]. Considering the error between ideal model and actual use, the response times were monitored in the ice-water conditioned environment.

Figure 6b and c show the thermal time constant τ of S1 and S2, which is 63.2% of the time required to change when the ambient temperature changes from 25 to 0 °C rapidly. It is calculated that τ values are about 345 and 11 ms for MCNO films sputtered on SiO₂/Si and SiO₂/PS/Si substrates by the following Eqs. (3) and (4): [43]

$$P = IV = K(T - T_0), \quad (3)$$

$$\tau = K/C, \quad (4)$$

where P is the power dissipated in the thin film samples (I is the constant current about 100 mA), T is the thin film temperature and T_0 the ambient temperature. K is the dissipation constant of MCNO film samples, and the C is the thermal capacity of MCNO samples. The PS buffer layer can effectively isolate the heat transfer between the ceramic film and the substrate due to the air stored in the pores of the oxidized porous silicon forms a thermal resistance layer. This leads to a reduction in the thermal capacity, which reduce the response time of the thermistor.

4 Conclusions

In summary, we have studied the influence of porous silicon buffer layer on crystal structure, optical and electrical properties, as well as the response time in MCNO thin film thermistors. The results and analysis leads to the following conclusions: (a) The porous silicon buffer layer did not have a significant effect on the crystallinity, texture and cation distribution of the MCNO film. However, the MCNO spinel film grown on the classical SiO₂/Si substrate within more flatness is superior to that prepared on SiO₂/PS/Si substrate in density and flatness. (b) The refractive index of MCNO/SiO₂/PS/Si films is only half of MCNO/SiO₂/Si in the range of 300–850 cm⁻¹, while the extinction coefficient is twice as high as MCNO/SiO₂/Si films. The NTC characteristics of the two samples show little difference in the thermal constants (3515 and 3469 K) even the high-frequency vibration experiments employed. (c) The result of the experiment and evaluation shows that films within PS layer captures an order of magnitude reduction in response time (11 ms) than the MCNO deposited on SiO₂/Si (345ms). The PS buffer layer can effectively achieve the thermal insulation between the NTC film and the Si-based substrate, and the introduction of porous silicon layer effectively improves the temperature responsive properties by reducing heat transfer. This research will provide experience for the preparation of thermosensitive thin films and useful information for fabricating fast response temperature sensors in the development of next generation information technology.

Author contributions

BY: Conceptualization, methodology, software, investigation, formal analysis, writing—original draft; YS: investigation, visualization; XW: data curation; ZC: validation; PZ : visualization, writing—review and editing; AC: resources, supervision; BG: validation; WK: conceptualization, funding acquisition, resources, supervision, writing—review and editing.

Funding

This work was supported by The Xinjiang Key Laboratory Foundation (Grant No. 2020D04043), The Youth Innovation Promotion Association CAS (Grant No. 2021433), and The Natural Science Foundation of Xinjiang Uygur Autonomous Region (Grant Nos. 2021D01D03 and 2022D01D03).

Data availability

The datasets generated and analysed during the current study are available from the corresponding author on reasonable request.

Declarations

Competing interests The authors have no relevant financial or non-financial interests to disclose. The authors have no relevant financial or non-financial interests to disclose.

References

1. D.P. Zhang, J. Wang, Y.J. Wang, X. Dai, A fast response temperature sensor based on fiber Bragg grating. *Meas. Sci. Technol.* **25**(7), 075105 (2014). <https://doi.org/10.1088/0957-0233/25/7/075105>
2. J.H. Wen, J. Wang, L. Yang, Y.F. Hou, D.H. Huo, E.L. Cai, Y.X. Xiao, S.S. Wang, Response time of microfiber temperature sensor in liquid environment. *IEEE Sens. J.* **20**(12), 6400–6407 (2020). <https://doi.org/10.1109/jsen.2020.2976535>
3. F. Zhang, Z. Huang, Effect of substrate thermal conductivity on the properties of Mn–Co–Ni–O thin film thermo-sensitive infrared detector. *Phys. Status Solidi A.* (2018). <https://doi.org/10.1002/pssa.201800040>

4. J. Xu, Y. Yin, H. Chen, Waterproof wearable sensing electronics of thin film with high stretchability, high temperature sensitivity and low cost. *J. Mater. Sci.: Mater. Electron.* **32**(17), 22654–22667 (2021). <https://doi.org/10.1007/s10854-021-06750-4>
5. X.C. Liu, M. Hu, Y.F. Wang, J.F. Liu, Y.X. Qin, High sensitivity NO₂ sensor based on CuO/p-porous silicon heterojunction at room temperature. *J. Alloys Compd.* **685**, 364–369 (2016). <https://doi.org/10.1016/j.jallcom.2016.05.215>
6. B.W. Yang, M. He, K.H. Wen, D.P. Xiong, Y.F. Feng, S.W. Ta, Z. Yang, Comparison of morphology, electrical properties and sensitivity between bulk and thin-film Mn_{1.5}Co₁Ni_{0.5}O₄ thermistors. *Ceram. Int.* **46**(17), 27134–27142 (2020). <https://doi.org/10.1016/j.ceramint.2020.07.192>
7. Y. Yu, S. Li, X. Wang, P. Chen, F. Liu, Y. Hou, Growth of Mn–Co–Ni–O nanowires by pulsed laser deposition. *Mater. Lett.* (2022). <https://doi.org/10.1016/j.matlet.2022.132287>
8. J. Mao, S. Wang, T. Xuan, Y. Song, B. Gao, A. Chang, W. Kong, High-solid content, low viscosity and long-term stability Mn–Co–Ni–O ceramic slurry for the fabrication of free-standing ultrathin NTC sheets. *Ceram. Int.* **48**(19), 27493–27500 (2022). <https://doi.org/10.1016/j.ceramint.2022.06.042>
9. L. Fan, J. Yao, P. Huo, B. Wang, Z. Liu, P. Zhao, A. Chang, J. Wang, Design and synthesis of thermistor materials with high aging stability: multicomponent equiatomic Mn–Co–Ni–Al–Zn–O ceramics. *Mater. Sci. Semicond. Process.* (2023). <https://doi.org/10.1016/j.mssp.2022.107263>
10. P.S. Chauhan, R. Kant, A. Rai, A. Gupta, S. Bhattacharya, Facile synthesis of ZnO/GO nanoflowers over Si substrate for improved photocatalytic decolorization of MB dye and industrial wastewater under solar irradiation. *Mater. Sci. Semicond. Process.* **89**, 6–17 (2019). <https://doi.org/10.1016/j.mssp.2018.08.022>
11. D.H. Cuate-Gomez, A. Garzon-Roman, J.L. Sosa-Sanchez, C. Zuniga-Islas, M.A. Dominguez, Polycrystalline Erbium Phthalocyanine Thin films deposited on silicon and porous silicon by ultrasonic spray pyrolysis: optical, morphological, and electrical characterizations. *J. Electron. Mater.* **50**(12), 6951–6963 (2021). <https://doi.org/10.1007/s11664-021-09264-1>
12. K.Y. Gu, Z.L. Zhang, K. Tang, J. Huang, Y. Shang, Y. Shen, M.Y. Liao, L.J. Wang, Effect of a seed layer on microstructure and electrical properties of Ga₂O₃ films on variously oriented Si substrates. *Vacuum* (2022). <https://doi.org/10.1016/j.vacuum.2021.110671>
13. Z.R. Chen, H.Y. Nan, Z. Liu, X.Y. Wang, X.F. Gu, S.Q. Xiao, Effect of thermal conductivity of substrate on laser-induced phase transition of MoTe₂. *J. Raman Spectrosc.* **50**(5), 755–761 (2019). <https://doi.org/10.1002/jrs.5559>
14. Y.P. Lan, Y.G. Zou, X.H. Ma, Y.B. Shi, J. Fan, Y.N. Hai, X.L. Wang, J.J. Yang, Q.H. Feng, Fabrication and characterization of dual coordinate self examined thermal flow sensor arrays based on longitudinal heat conduction. *IEEE Sens. J.* **20**(1), 434–440 (2020). <https://doi.org/10.1109/jksen.2019.2941531>
15. T.Y. Ma, Y.P. Wang, J.Z. Zhou, A Si-based suspended tunnel structure with trapezoidal section by two-step etching. *J. Micromech. Microeng.* (2022). <https://doi.org/10.1088/1361-6439/ac4460>
16. Z.Q. Wang, M. Kimura, N. Inomata, J.H. Li, T. Ono, Compact micro thermal sensor based on silicon thermocouple junction and suspended fluidic channel. *IEEE Sens. J.* **20**(19), 11122–11127 (2020). <https://doi.org/10.1109/jksen.2020.2997926>
17. N.F. Zhao, A.R. Mao, Z.Y. Shao, H. Bai, Anisotropic porous ceramic material with hierarchical architecture for thermal insulation. *Bioinspiration Biomim.* (2022). <https://doi.org/10.1088/1748-3190/ac3216>
18. T. Shi, J. Liang, X. Li, C. Zhang, H. Yang, Improving the corrosion resistance of aluminum alloy by creating a superhydrophobic surface structure through a two-step process of etching followed by polymer modification. *Polymers* (2022). <https://doi.org/10.3390/polym14214509>
19. X.H. Li, Z.C. Yang, H.L. Shao, K.F. Li, Z.F. Fei, The influence of chopped PI fibers on thermal, mechanical and sound insulation properties of methylsilsesquioxane aerogels. *J. Sol-Gel Sci. Technol.* **101**(3), 519–528 (2022). <https://doi.org/10.1007/s10971-021-05701-z>
20. X.S. Zhang, Q. Tian, B. Wang, N. Wu, C. Han, X. Long, Y.D. Wang, Flexible porous SiZrOC ultrafine fibers for high-temperature thermal insulation. *Mater. Lett.* **299**, 130131 (2021). <https://doi.org/10.1016/j.matlet.2021.130131>
21. J. Kwon, J. Kim, D. Park, H. Han, A novel synthesis method for an open-cell microsp sponge polyimide for heat insulation. *Polymer.* **56**, 68–72 (2015). <https://doi.org/10.1016/j.polymer.2014.06.090>
22. S.P. Gaur, P. Kumar, K. Rangra, D. Kumar, Efficient thermal utilization in MEMS bulk micromachined pyroelectric infrared sensor using thermal oxide thin layer. *Microsyst. Technol.* **24**(3), 1603–1608 (2018). <https://doi.org/10.1007/s00542-017-3560-0>
23. H. Lu, M.L. Jin, Z.B. Zhang, S.J. Wu, L.L. Shui, Wafer-scale fabrication and transfer of porous silicon films as flexible nanomaterials for sensing application. *Nanomater.* **12**(7), 1191 (2022). <https://doi.org/10.3390/nano12071191>
24. T. Thomas, Y. Kumar, J.A.R. Ramon, V. Agarwal, S.S. Guzman, R. Reshmi, S. Pushpan, S.L. Loreda, K.C. Sanal, Porous silicon/alpha-MoO₃ nanohybrid based fast and highly sensitive CO₂ gas sensors. *Vacuum.* **184**, 109983 (2021). <https://doi.org/10.1016/j.vacuum.2020.109983>
25. T.T. Xuan, J.Z. Yan, J.H. Wang, W.W. Kong, A.M. Chang, Characterization of Al-doped Mn–Co–Ni–O NTC thermistor

- films prepared by the magnetron co-sputtering approach. *J. Alloys Compd.* (2020). <https://doi.org/10.1016/j.jallcom.2020.154831>
26. X.B. Wang, W.W. Kong, D.L. He, T.T. Xuan, J.H. Mao, B. Gao, A.M. Chang, Substrate-induced morphology and its effect on the electrical properties and stability of polycrystalline $Mn_{1.2}Co_{1.5}Ni_{0.3}O_4$ thin films. *J. Mater. Sci.: Mater. Electron.* **32**(17), 22588–22598 (2021). <https://doi.org/10.1007/s10854-021-06744-2>
 27. W.W. Kong, J.H. Wang, J.C. Yao, A.M. Chang, Influence of oxygen atmosphere annealing on the thermal stability of $Mn_{1.2}Co_{1.5}Ni_{0.3}O_{4\pm\delta}$ ceramic films fabricated by RF magnetron sputtering. *Ceram. Int.* **44**(2), 1455–1460 (2018). <https://doi.org/10.1016/j.ceramint.2017.10.040>
 28. K. Zhang, W.W. Kong, Q. Wang, T.T. Xuan, F.P. Cheng, A.M. Chang, Effect of substrate temperature on structure, cationic distribution and electrical properties of $MnCo_{0.2}Ni_{0.1}Mg_{0.6}Al_{1.1}O_4$ thin films. *J. Mater. Sci.: Mater. Electron.* **30**(15), 14200–14206 (2019). <https://doi.org/10.1007/s10854-019-01787-y>
 29. T.T. Wei, L. Chen, H.H. Fu, Y.L. Shi, J. Hou, F. Yu, J.H. Ye, H.Q. Li, C.C. Fan, D.H. Chen, B. Dai, Synthesis and formation mechanism of monodisperse Mn–Co–Ni–O spinel nanocrystallines. *Adv. Powder Technol.* **30**(7), 1269–1276 (2019). <https://doi.org/10.1016/j.apt.2019.02.002>
 30. Q. Shi, W. Ren, W.W. Kong, L. Wang, C. Ma, J.B. Xu, A.M. Chang, C.Q. Jiang, Oxidation mode on charge transfer mechanism in formation of Mn–Co–Ni–O spinel films by RF sputtering. *J. Mater. Sci.: Mater. Electron* **28**(18), 13659–13664 (2017). <https://doi.org/10.1007/s10854-017-7208-8>
 31. M. Kim, X.M. Chen, X. Wang, C.S. Nelson, R. Budakian, P. Abbamonte, S.L. Cooper, Pressure and field tuning the magnetostructural phases of Mn_3O_4 : Raman scattering and x-ray diffraction studies. *Phys. Rev. B: Condens. Matter.* **84**(17), 174424 (2011). <https://doi.org/10.1103/PhysRevB.84.174424>
 32. E. Zielony, R. Szymon, A. Wierzbička, A. Reszka, M. Sobanska, W. Pervez, Z.R. Zytewicz, Strain and lattice vibration mechanisms in $GaN-Al_xGa_{1-x}N$ nanowire structures on Si substrate. *Appl. Surf. Sci.* **588**, 152901 (2022). <https://doi.org/10.1016/j.apsusc.2022.152901>
 33. W.W. Kong, B. Gao, C.P. Jiang, A.M. Chang, Influence of the oxygen pressure on the preferred orientation and optical properties of the pulsed-laser deposited $Mn_{1.56}Co_{0.96}Ni_{0.48}O_{4\pm\delta}$ thin films. *J. Alloys Compd.* **650**, 305–310 (2015). <https://doi.org/10.1016/j.jallcom.2015.07.257>
 34. M. Gartner, M. Stoica, M. Nicolescu, H. Stroescu, The ellipsometry versatility in the study of sol–gel films. *J. Sol–Gel Sci. Technol.* **98**(1), 1–23 (2021). <https://doi.org/10.1007/s10971-021-05504-2>
 35. S. Checcucci, T. Bottein, M. Gurioli, L. Favre, D. Grosso, M. Abbarchi, Multifunctional metasurfaces based on direct nanoimprint of titania sol–gel coatings. *Adv. Opt. Mater.* (2019). <https://doi.org/10.1002/adom.201801406>
 36. R.F. Li, Q.Y. Fu, X.H. Zou, Z.P. Zheng, W. Luo, L. Yan, Mn–Co–Ni–O thin films prepared by sputtering with alloy target. *J. Adv. Ceram.* **9**(1), 64–71 (2020). <https://doi.org/10.1007/s40145-019-0348-y>
 37. B. Wang, J.C. Yao, J.H. Wang, A.M. Chang, Valence-induced distortion controls the resistivity and thermal stability of $Co_{2.77}Mn_{1.71}Fe_{1.10}Zn_{0.42}O_8$ ceramics. *Mater. Des.* (2020). <https://doi.org/10.1016/j.matdes.2020.108736>
 38. Z.L. Fu, H.C. Nie, Y.X. Wei, B. Zhang, A.M. Chang, Effect of Mn-doping on microstructure and electrical properties of $La_{2/3}Cu_3Ti_4O_{12}$ ceramics. *J. Alloys Compd.* **847**, 156 (2020). <https://doi.org/10.1016/j.jallcom.2020.156525>
 39. B. Wang, J.H. Wang, J.C. Yao, A.M. Chang, An innovative approach to design highly stabilized thermistor materials: dual-phase five-component $CoMnFeZnYO_7$ ceramics. *J. Mater. Chem. C* **9**(5), 1794–1803 (2021). <https://doi.org/10.1039/d0tc05422d>
 40. X.M. Li, L. Chen, J. Hou, P.J. Zhao, B. Gao, Q. Zhao, A.M. Chang, Q. Shi, W.W. Kong, Improving the sensitivity of $LaMnO_3$ NTC films by Al ion implantation. *Vacuum* **208**, 111704 (2023). <https://doi.org/10.1016/j.vacuum.2022.111704>
 41. Y.X. Song, S. Wang, B. Gao, A.M. Chang, W.W. Kong, Development of a highly sensitive and stable flexible temperature sensor based on all-inorganic Mn–Co–Ni–O thin films. *Adv. Mater. Interfaces* (2023). <https://doi.org/10.1002/admi.202202274>
 42. G. Gesele, J. Linsmeier, V. Drach, J. Fricke, R. ArensFischer, Temperature-dependent thermal conductivity of porous silicon. *J. Phys. D: Appl. Phys.* **30**(21), 2911–2916 (1997). <https://doi.org/10.1088/0022-3727/30/21/001>
 43. Q. Wang, W. Kong, J. Yao, A. Chang, Fabrication and electrical properties of the fast response $Mn_{1.2}Co_{1.5}Ni_{0.3}O_4$ miniature NTC chip thermistors. *Ceram. Int.* **45**(1), 378–383 (2019). <https://doi.org/10.1016/j.ceramint.2018.09.177>

Publisher's Note Springer nature remains neutral with regard to jurisdictional claims in published maps and institutional affiliations.

Springer Nature or its licensor (e.g. a society or other partner) holds exclusive rights to this article under a publishing agreement with the author(s) or other rightsholder(s); author self-archiving of the accepted manuscript version of this article is solely governed by the terms of such publishing agreement and applicable law.